

The spacer cations interplay for efficient and stable layered two-dimensional perovskite solar cells

Ning Zhou^{a+}, Bolong Huang^{b+}, Mingzi Sun^b, Yu Zhang^a, Liang Li^a, Yingzhuo Lun^d, Xueyun Wang^d, Jiawang Hong^d, Qi Chen^c, Huanping Zhou^{a*}

a. Beijing Key Laboratory for Theory and Technology of Advanced Battery Materials, Department of Materials Science and Engineering, College of Engineering, Peking University No.5 Yiheyuan Road Haidian District, Beijing 100871, P. R. China

b. Department of Applied Biology and Chemical Technology, Hong Kong Polytechnic University, Hung Hom, Kowloon, Hong Kong, P. R. China

c. School of Materials Science and Engineering, Beijing Institute of Technology, 5 Zhongguancun South Street, Beijing 100081, P. R. China

d. School of Aerospace Engineering, Beijing Institute of Technology, 5 Zhongguancun South Street, Beijing 100081, P. R. China

+ Authors contribute equally to this work

Keywords: 2D perovskites, exciton binding energy, solar cells, organic spacer, efficiency

Abstract

Organic spacer cations in layered two-dimensional (2D) $((A_1)_2(A_2)_{n-1}B_nX_{3n+1})$ perovskite materials improve the long-term stability of resulting solar cells, but hamper their power conversion efficiency due to poor carrier generation/transportation. It thus requires rational guidelines to design organic spacer cations employed. Different from one-component A_1 cation spacer system, we employ the mixed A_1 cations in the layered 2D perovskites to investigate the interplay between alkylamine cation and unsaturated alkylamine cations with long-range p - π coupling effects. It is revealed that alkylamine spacer cations are flexible to facilitate precursor assembly, which results in the orientated growth of perovskite crystals. Unsaturated alkylamine cations further lead to reduced exciton binding energy, which improves carrier pathway in the 2D perovskites. By mixing both cations, we observe substantially improved open circuit voltage in the resultant photovoltaic cells with the efficiency of 15.46%, one of the highest one based on $(A_1)_2(A_2)_3Pb_4I_{13}$ layered 2D perovskites. The generality of the design principle is further extended to other cation combinations.

1. Introduction

Hybrid organic-inorganic halide perovskites have been emerged as promising semiconductors for the applications in solar cells, photodetectors, light-emitting diodes, and lasers, etc.¹ The power conversion efficiency (PCE) of perovskite-based solar cells (PSCs) has rapidly boosted to 23.7%² within a short period of time, due to their outstanding properties including high extinction coefficient³, appropriate band gap⁴, long charge diffusion length⁵ and high defects tolerance. However, the most efficient perovskite solar cells still suffer from the most intractable degradation issue that hampers their further commercialization.⁶ Tremendous efforts have been devoted to prolong the long-term stability of devices, e.g. the design of absorbers^{7,8}, the employment of advanced carrier transport materials/electrodes⁹, as well as the development of encapsulation techniques¹⁰. In view of current advance in perovskite solar cells, to improve the intrinsic stability of perovskite layer during its operation condition is urgently needed.

Ruddlesden–Popper layered perovskite with longer hydrophobic alkyl chains and weaker polarity have been demonstrated to largely enhance the moisture stability in the resultant photovoltaic devices.^{11–15} However, the exciton binding energy of layered 2D perovskite ($(A_1)_2(A_2)_{n-1}B_nX_{3n+1}$) is much larger than that of the 3D (ABX_3) counterparts⁵, due to the dielectric modulation between the organic cations and the dimensionality of the inorganic framework.¹⁶ Such a large exciton binding energy (several hundred meV) substantially affects the exciton dissociation in the electrical field.⁵ Meanwhile, the large organic cations (A_1), which act as insulating spacing layers between conductive inorganic slabs, inhibit charge transport between neighboring inorganic layers. These two factors are considered as the primary origin for the relatively lower efficiency in solar cells based on 2D perovskites.^{13,17} To this respect, a better control on the crystal orientation and the composition within layered 2D structure is proven to be effective to manipulate the carrier transportation. For instance, by casting solution on a hot substrate, the crystal orientation in the $(BA)_2(MA)_3Pb_4I_{13}$ ($BA^+ = C_4H_9NH_3^+$) layered 2D perovskite film can be well-controlled to form an efficient charge transport layer along the out-of-plane direction and therefore yield an improved photovoltaic performance with a PCE of 12.5%.¹³ Through FA^+ or Cs^+ incorporation in the A_2 site, a reduced carrier recombination rate in the doped $(BA)_2(MA)_3Pb_4I_{13}$ films and promoted device performance have been achieved.^{18,19} While the above work suggests the effectiveness of A_2 cation substitution, it still lacks the A_1 cation rational design in layered 2D materials from molecule level to tune the structural and optoelectronic properties. In particular, given that the A_1 cations are crucial to the self-assembly and quantum confinement behavior in layered 2D materials,^{20,21} a profound understanding on the A_1 cations is urgently needed, which will promote the carrier generation and transportation to benefit the resulting device performance eventually.

Here, we firstly employed the combination of PEA^+ ($C_6H_5(CH_2)_2NH_3^+$) and BA^+ as a typical model, to implement mixed A_1 cations in layered 2D perovskites, wherein the interplay between unsaturated alkylamine and alkylamine cations is investigated carefully. The phase, crystallization behavior and optoelectronic properties of a series of $(BA,PEA)_2(MA)_3Pb_4I_{13}$ were examined systematically in the context of experimental characterization and theoretical calculation. Without disturbing the orientated structure or introducing extra defects, the incorporation of 10% PEA in $BA_2MA_3Pb_4I_{13}$ layered 2D perovskite yields a PCE of 15.46%, one of the highest efficiency based on $(A_1)_2(A_2)_3Pb_4I_{13}$ perovskites so far. We generalized the finding to other unsaturated alkylamine cations, such as 1-naphthalene ethylamine (NEA), allylammonium (ALA), propargylamine (PGA). Such cations are found to improve carrier transport across the absorber layer, and on the other hand, long-chain alkylamine cations (BA^+) facilitate precursor assembly and orientated crystal growth. Furthermore, the combination of experimental results and density functional theory (DFT) calculations proved that PEA^+ with long-range p- π coupling effect in $(BA,PEA)_2(MA)_3Pb_4I_{13}$ could effectively decrease the exciton binding energy via electronic distribution migration.

2. Results and Discussion

2.1 Material Characterizations

We aim to modulate the spacer layer composition for intrinsically improving the carrier generation and transportation. Among different large organic cations, BA and PEA are most often used for retaining the Ruddlesden–Popper structure. However, BA and PEA are quite different in the aspect of molecular and electronic structure. BA molecule has a long alkyl chain, while PEA molecule is relatively “rigid” with aromatic long-ranged p- π coupling effect. Accordingly, BA based layered 2D perovskite is expected to assemble into highly crystal orientation structure, and the unique electronic structure of PEA may benefit the carrier behavior modulation. Therefore, we used PEA⁺ and BA⁺ as an example to illustrate the structural and the optoelectronic properties of 2D-perovskites and the corresponding solar cells based on the combination of the two kinds spacers.

To obtain (BA_{1-x}PEA_x)₂(MA)₃Pb₄I₁₃ ($x = 0, 0.1, 0.2, 0.4, 0.8$ and 1.0) family of layered 2D perovskite compounds, we gradually replaced BA⁺ with PEA⁺ according to the given stoichiometric ratio. The detailed fabrication process was illustrated in the experimental section, which is similar to the previous report.¹³ To simplify the chemical formula, we used PEA0.0, PEA0.1, PEA0.2, PEA0.4, PEA0.8 and PEA1.0 to represent (BA_{1-x}PEA_x)₂(MA)₃Pb₄I₁₃ $x=0, 0.1, 0.2, 0.4, 0.8$ and 1.0 , respectively. Scanning electron microscopy (SEM) and atomic force microscopy (AFM) measurements are then used to study the morphology of (BA,PEA)₂(MA)₃Pb₄I₁₃ series perovskite films. As displayed in **Figure S1**, PEA0.0, PEA0.1 and PEA0.2 film possess densely packed grains and smooth surface. This is in line with the observed strong space confined effect in layered 2D perovskite materials.²⁰ When substituting BA⁺ with 40% or more PEA, the grains are still densely packed but the surface roughness becomes larger. The AFM images of perovskite films are shown in **Figure S2**. The root-mean-square (RMS) roughness of the PEA0.0, PEA0.1, PEA0.2 films across a scanned area of $5 \times 5 \mu\text{m}^2$ were determined to be 6.90, 5.32 and 4.78 nm, respectively, suggesting the superior film quality of PEA0.1 and PEA0.2. While the RMS roughness of PEA0.4, PEA0.8 and PEA1.0 films were 7.36, 36.18 and 44.81 nm, respectively, probably stemming from the relatively weak space confined effect.

We investigated the crystal phase and orientation of the (BA,PEA)₂(MA)₃Pb₄I₁₃ series perovskite films by using X-ray diffraction (XRD) measurement and synchrotron grazing-incidence wide-angle X-ray scattering (GIWAXS) analysis, respectively. Two dominant diffraction peaks were observed at diffraction angles (2θ) of $14.2^\circ, 28.4^\circ$, representing the (111), (222) crystallographic planes of layered 2D perovskite, respectively (**Figure 1a**).¹⁹ When PEA⁺ gradually replaces BA⁺, the diffraction angle doesn't shift appreciably. It indicates that no obvious variation in crystal lattices. We integrated (111) and (222) diffraction peak area, and the detailed data are listed in **Table S1**. Obviously, compared to BA dominant film, PEA dominant film leads to substantially decreased crystallinity of the perovskite film. Also, the higher the PEA⁺ concentration, the weaker of the (222) diffraction peak, as depicted in **Figure 1b**. This indicated that the PEA was likely to affect the crystallization kinetics during film formation, leading to the decreased crystallinity, as well as altered film growth direction. We then used GIWAXS analysis to further confirm the above phenomenon. The scattering patterns of the (BA,PEA)₂(MA)₃Pb₄I₁₃ films with different PEA ratio are shown in **Figure 1d–i**. All the samples exhibit sharp and discrete Bragg spots, indicating the highly oriented crystal grain. The

increased intensity of (111) plane accompanying with the decrease of (222) plane affirmed the changed crystal growth kinetics in layered 2D structure induced by PEA. Moreover, we integrated the GIWAXS pattern azimuthally over the ring at $q_{xy} \sim -0.25 \text{ \AA}^{-1}$ to 0.25 \AA^{-1} . As depicted in **Figure 1c**, the higher the PEA concentration, the weaker of the crystallinity, which is in accordance with the XRD analytics above. To be noted, when PEA^+ concentration is higher than 20%, the degree of orientation was decreased, which means PEA^+ would weaken the assembly process. This further suggests that the long-chain alkylamine cations BA^+ primarily contributed to the assembled orientated structure, and the incorporation of low concentration PEA^+ can preserve the pristine structure.

The photoluminescence (PL) emission property of $(\text{BA,PEA})_2(\text{MA})_3\text{Pb}_4\text{I}_{13}$ series perovskite films were further studied. All the films were spin-coated on the glass substrate. The peak intensity was normalized to better clarify the exact emission wavelength shift induced by doping. When the laser beam hit the perovskite from both the film and glass side, multiple PL emission peaks were observed, representing different n phases in layered 2D perovskites (**Figure 2a-b**). However, when the laser beam illuminated from the glass side, the small n value phases were more obvious when compared to that of the opposite case. This is consistent with recently reported work.^{19,21} Additionally, the strong PL emission peak in **Figure 2a** (generally defined as $n=\infty$) showed gradual blue-shift from 752 nm to 748 nm for PEA0.0 and PEA0.1, respectively. However, when the ratio of PEA further increased to 0.2-1.0, the PL emission exhibited red shift, as shown in the insert of **Figure 2a**. In general, the introduction of PEA in the BA based layered 2D perovskite materials can lower the bandgap, resulting in a gradual red shift of the PL emission peak. While the abnormal blue shift of PL peak observed in PEA0.1 film was attributed to the disturbance of original BA orbital distribution and strong exciton-inhibition by PEA incorporation, which will be described in the following in detail. We then employed time-resolved photoluminescence (TRPL) spectroscopy measurement to detect the carrier lifetime of PEA0.0 and PEA0.1 film. The fluorescence signals were fitted by two exponentials, as indicated in **Figure 2c**. The emission of PEA0.1 perovskite film decayed with a relatively longer lifetime of 12.52 ns, as compared to that of the PEA0.0 film with 8.68 ns. It implies a suppressed non-radiative recombination rate, which is likely associated to a decreased trap density in the film induced by PEA incorporation.

Furthermore, we measured photoluminescence quantum yield (PLQY) of the films and determined the corresponding optoelectronic quality (χ). **Figure 2d** shows the PLQY results for PEA0.0 and PEA0.1 films, the higher PLQY of PEA0.1 means the trap-mediated non-radiative recombination has been suppressed. According to previous report,²² the quasi fermi level splitting (QFLS or $\Delta\mu$) can be related to the external photoluminescence yield (PLQY_{Ext}) with the expression: $\Delta\mu = \Delta\mu_{\text{max}} - kT \ln \frac{1}{\text{PLQY}_{\text{Ext}}}$ (1), where $\Delta\mu_{\text{max}}$ is the QFLS in the radiative limit, and can be simply calculated using the formula $0.932E_g - 0.167$.²³ Note that both $\Delta\mu$ and $\Delta\mu_{\text{max}}$ depend on the bandgap, temperature, and the illumination intensity as well. Herein, the corresponding parameters for perovskite films were measured at 300 K under 1 sun AM1.5G illumination. We calculated the material quality parameter χ , which is the ratio of $(\Delta\mu/\Delta\mu_{\text{max}})$ to capture the true optoelectronic quality of any given composition with defined bandgap. Accordingly, the optoelectronic

quality χ is determined to be 94.2% for PEA0.0 film and 96.0% for PEA0.1 film (**Figure 2e**). The detailed parameters are summarized in **Table S2**. This further demonstrates that the material quality has been improved successfully by PEA incorporation. To access the film trap density, we carried out space charge limited current (SCLC) measurement (**Figure 2f**) based on ITO/PEDOT:PSS/perovskite/Spiro-OMeTAD/Au devices.¹⁸ The trap density n_t was calculated according to the relation: $n_t = \frac{V_{TFL}\epsilon\epsilon_0}{eL^2}$, where V_{TFL} is the trap-filled limit voltage, ϵ_0 is the vacuum permittivity, and e is the electron charge, L is the thickness of the film. According to the cross-sectional SEM image of the device (**Figure S3**), the thicknesses of the perovskite is approximately 350 nm. By adopting ϵ of 25,¹⁸ the trap density n_t for PEA0.0 and PEA0.1 films were determined to be $1.87 \times 10^{16} \text{ cm}^{-3}$ and $1.58 \times 10^{16} \text{ cm}^{-3}$ respectively. Accordingly, the hole mobility was also measured to be $1.55 \times 10^{-3} \text{ cm}^2 \text{ V}^{-1} \text{ s}^{-1}$ and $2.07 \times 10^{-3} \text{ cm}^2 \text{ V}^{-1} \text{ s}^{-1}$ for PEA0.0 and PEA0.1 films. The relatively lower trap density and larger mobility of PEA0.1 film suggest its better film quality than that of PEA0.0.

2.2 Device Performance and Energy Band Alignment

We employed the PEA0.0 and PEA0.1 based perovskites as absorber materials in solar cells. **Figure 3a** illustrates the device structure and **Figure S3** is the cross-sectional SEM image of the device. We adopted a planar inverted architecture of ITO/PEDOT:PSS/Perovskite/PCBM/BCP/Ag to fabricate solar cells by considering the energy band matching.^{12,21} All devices were prepared according to the experimental section. **Figure 3b** shows the J–V characteristics of the best performing devices under simulated AM1.5G irradiation (100 mW/cm^2). **Table 1** summarizes the photovoltaic performance. The device based on PEA0.0 film yields a power conversion efficiency (PCE) of 11.71% with an open-circuit voltage (V_{oc}) of 0.988 V, a short circuit current density (J_{sc}) of 16.11 mA cm^{-2} and a fill factor (FF) of 73.56%. The PEA0.1 based perovskite device achieves an improved PCE of 15.46%, with $V_{oc} = 1.182 \text{ V}$, $J_{sc} = 17.12 \text{ mA cm}^{-2}$ and $FF = 76.40\%$. The hysteresis phenomenon is negligible in the layer 2D perovskite solar cells as shown in **Figure S4** and **Table S3**. To our understanding, this is one of the highest efficiency regarding layered 2D ($n=4$) based perovskite solar cell. The corresponding PCE from steady state power output measurement of PEA0.1 based device is 14.90%, while the device based on PEA0.0 is 11.39%, as shown in **Figure 3c**. **Figure S5** summarized the V_{oc} , J_{sc} , FF, PCE statistic distribution of a number of ten PEA0.0 and PEA0.1 based solar cells, respectively. The typical incident photon to current conversion efficiency (IPCE) spectra are shown in **Figure 3d**, wherein the integrated current value is 16.45 mA/cm^2 for PEA0.1 based cell, which is higher than that of the PEA0.0 based cell of 16.02 mA/cm^2 . We also carried out J–V characteristics under different incident light intensities ranging from 100 to 50 mW/cm^2 (from 1 to 0.5 sun), as shown in **Figure S6**. The ideality factor for both cell are greater than 1, indicating that the recombination is largely limited by trap-assisted Shockley–Read–Hall (SRH) recombination.²⁴ A decrease in ideality factor from 1.63 to 1.51 is observed upon the incorporation of 10% PEA in the absorber compared to that of PEA0.0. This means the trap-assisted SRH recombination is suppressed in PEA0.1 based films, which agrees with its reduced trap states. It's also in accordance to the TRPL and SCLC measurement above. We evaluated the device stability by recording the steady state output PCE under constant illumination, where the devices retained $\sim 80\%$ of their original efficiency after 700 h, as

shown in **Figure 3e**. The excellent long term maximum power point stability in layered 2D perovskite may attribute to the suppressed ion migration because of the increase in the energy required to form an ion vacancy, compared to 3D counterpart.²⁵ Meanwhile, we examined the PEA0.1 based perovskite solar cells stability by storing in glove box, under one sun illumination, or under a temperature of 85 °C, respectively, without encapsulation. (**Figures S7-S9**). The devices maintained over 92% and 95% of the original PCEs, after 7000 h storage and 1200 h continuous one sun illumination, respectively. When stored the device in glove box at 85 °C, the initial PCEs maintained over 80% after 120 h. It indicates that the layered 2D devices possess excellent operational durability under light illumination, as well as good thermal stability.

The kelvin probe force microscopy (KPFM) technique was employed to investigate the surface potential difference of PEA0.0 and PEA0.1 perovskite films, which was associated with the work function with respect to the vacuum energy level. As shown in **Figure S10a-b**, the work functions of the perovskite films are derived from the contact potential difference (CPD) between a Pt-coated conductive cantilever probe and the samples. Accordingly, the PEA0.1 perovskite film shows a lower average CPD (-71 mV) than that (-32 mV) of PEA0.0 perovskite film (**Figure S10c**), indicating an upward shift of Fermi level after incorporation of 10% PEA. We also conducted ultraviolet photoelectron spectroscopy (UPS) to determine the molecule energy level by measuring the energy distribution of the photoelectron excited by the ultraviolet light. The work functions are determined to be 4.2 eV and 4.15 eV, respectively (**Figure S11**). Benefiting from the shallower Fermi level, the PEA0.1 perovskite film may tend to exhibit a larger gap between the splitting of electron quasi-Fermi level (E_m) and hole quasi-Fermi level (E_{fp}) under light illumination, and thus a higher V_{oc} of the device. The upward-shifted E_f of PEA0.1 perovskite matches better with the HOMO level of PEDOT:PSS under illumination, leading to an optimized energy band alignment, as illustrated in **Figure S10d**.

2.3 The Generality of Spacer Interplay between Unsaturated Alkylamine and Alkylamine

To clarify the general applicability of the combination of the two different kind of cations to tune the electronic and structural properties, we introduced another three unsaturated alkylamine cations with strong long range p- π coupling effect, e.g. NEA⁺, ALA⁺, PGA⁺. The combinations include BA_{0.9}NEA_{0.1}, BA_{0.9}ALA_{0.1} and BA_{0.9}PGA_{0.1}, while pure NEA, ALA, PGA was used as the reference. As shown in **Figure 4a**, when NEA⁺ replaces BA⁺ completely, an orientated layered perovskite film can not form, probably due to the inferior self-assembly dynamics caused by the too large “rigid” ring. Similarly, when ALA⁺, PGA⁺ replaces BA⁺ completely, the degree of orientation was significantly reduced compared to that of BA₂MA₃Pb₄I₁₃ film, probably due to that ALA⁺, PGA⁺ cations are the more “rigid” than BA⁺. It therefore suggests that the relatively “rigid” cation could affect the film formation dynamics, resulting in less orientated and lower crystallized layered 2D film. However, when NEA⁺, ALA⁺, PGA⁺ partially replace BA⁺ with a ratio of 10%, the films exhibit high orientation and crystallinity, which is likely because that the BA long chain cation has superior structural flexibility to facilitate self-assembly and a small amount of “rigid” cation don’t substantially disturb the assembled structure.

With respect to the photoluminescence property, all $\text{NEA}_2\text{MA}_3\text{Pb}_4\text{I}_{13}$, $\text{ALA}_2\text{MA}_3\text{Pb}_4\text{I}_{13}$, $\text{PGA}_2\text{MA}_3\text{Pb}_4\text{I}_{13}$ perovskite films show red shift than $\text{BA}_2\text{MA}_3\text{Pb}_4\text{I}_{13}$ (**Figure 4b**), and abnormal blue shifts of PL peak are observed in all $\text{BA}_{0.9}\text{NEA}_{0.1}$, $\text{BA}_{0.9}\text{ALA}_{0.1}$, $\text{BA}_{0.9}\text{PGA}_{0.1}$ (**Figure 4c**). This phenomenon is in line with the above $(\text{BA},\text{PEA})_2\text{Pb}_4\text{I}_{13}$ system, which will be discussed later. We then fabricated devices using these six kinds of perovskites, and the device performance were summarized in **Figure 4d and 4e**. $\text{NEA}_2\text{MA}_3\text{Pb}_4\text{I}_{13}$, $\text{ALA}_2\text{MA}_3\text{Pb}_4\text{I}_{13}$, $\text{PGA}_2\text{MA}_3\text{Pb}_4\text{I}_{13}$ based device performance are quite poor with PCE less than 2%, probably because these films have reduced crystallinity and orientation. While, devices from $(\text{BA}_{0.9}\text{NEA}_{0.1})_2\text{MA}_3\text{Pb}_4\text{I}_{13}$, $(\text{BA}_{0.9}\text{ALA}_{0.1})_2\text{MA}_3\text{Pb}_4\text{I}_{13}$, $(\text{BA}_{0.9}\text{PGA}_{0.1})_2\text{MA}_3\text{Pb}_4\text{I}_{13}$ exhibited elevated Voc of 1.09 V, 1.03 V, 1.06 V, compared to a 0.97 V based on $\text{BA}_2\text{MA}_3\text{Pb}_4\text{I}_{13}$. Interestingly, among these three cations, NEA^+ has the strongest long range p- π coupling effect, and PGA^+ is the weakest, which is in accordance to the Voc variation. To be noted, although NEA has stronger long-range p- π coupling effect than PEA, its self-assembly capability is not as good as PEA(**Figure 4a**), leading to a slightly inferior Voc enhancement than that of $(\text{BA}_{0.9}\text{PEA}_{0.1})_2\text{MA}_3\text{Pb}_4\text{I}_{13}$ based perovskite solar cell. The PCE shows a similar trend with respect to the Voc (**Figure 4e**), as the combination of unsaturated alkylamine with p- π coupling effect and long-chain alkylamine cations primarily affects Voc, and has less impact on other parameters, e.g. Jsc and FF.

2.4 Modulation of Exciton Binding Energy

Especially, we adopted temperature-dependent PL measurement ranging from 350 K to 90 K to detect the carrier behavior of different n value phases in $\text{BA}_2\text{MA}_3\text{Pb}_4\text{I}_{13}$ and $(\text{BA}_{0.9}\text{PEA}_{0.1})_2(\text{MA})_3\text{Pb}_4\text{I}_{13}$ layered 2D perovskites. As shown in **Figure S12**, the PL emission peaks of n=2, n=3, and n= ∞ phase are located at about 565 nm, 610 nm, and 760 nm, respectively. It should be noted that when the temperature decreased, an additional peak at 590 nm appeared in the n=2 phase, which was attributed to either a phonon replica or surface bound excitons.²⁶⁻²⁸ In order to visualize the results, the normalized temperature dependent PL spectra were mapped in color-coded images, as shown in **Figure 5a-f**. Clearly, it was observed that the PL emission peaks of PEA0.0 and PEA0.1 films exhibited the similar variation tendency with the decreased temperature for n=2, n=3 and n= ∞ phases, respectively (**Figure S13**). For n=2 and n=3 phases, the peak positions of PL emission remained almost constant with only a slight blue shift as the temperature decreased, which was possibly caused by the electron-phonon coupling effect raised by self-trapped excitons. The nearly unchanged peak energy supports the argument of free exciton emission in layered 2D perovskites.^{26,29} For n= ∞ phase, it showed an obvious red shift when the temperature decreased from 350 K to 150 K. This had previously been observed in 3D perovskite, which could be attributed to effects from the negative Varshni parameter.^{26,29,30} In this temperature range, the intensity of the PL emission for n= ∞ phase increased with decreasing temperature as shown in **Figure S12**. This is probably due to the increased probability in the dissociation of free excitons and the change in material parameters in contrast to typical semiconductors.³¹ While further decreasing the temperature from 150 K to 130 K, an abnormal blue shift of PL was observed, accompanying with the appearance of a new peak nearby. This was attributed to the phase transition from the tetragonal to the orthorhombic phase of n= ∞ perovskites.³²⁻³⁴ The above phenomenon indicates that the coexisted multiphase (n=2, n=3 and n= ∞ phases) in layered 2D perovskite remain their original properties.

We further extracted the exciton binding energy of $n=2$, $n=3$, $n=\infty$ phases for both films, respectively, by analyzing the emission quenching behavior that was reflected by its temperature dependence of integral PL intensity. The integral PL intensity as a function of temperature was described in **Figure 5g-i**. While the fitting process follows the expression: $I_T = \frac{I_0}{1+Ae^{-E_B/k_B T}}$ (2), in which I_T is the integral PL intensity, I_0 is the intensity at 0 K, E_B the exciton binding energy, and K_B the Boltzmann constant. The derived exciton binding energy E_B of different n phases are listed in **Table 2**, which substantially impact the efficiency of exciton dissociation and charge transfer.³⁵ Interestingly, the exciton binding energy of PEA0.1 film is smaller than PEA0.0 film for all the $n=2$, 3 and ∞ phases. This implies that the electric field required to split the excitons is lower and exciton splitting at the corresponding interface is more efficient for PEA0.1 based device than that of PEA0.0. To be noted, the overall driving force to promote exciton dissociation and carrier transfer from the perovskite to adjacent transport materials is provided by the energy offset between the conduction-band minimum (E_C) of perovskite and the lowest unoccupied molecule orbital (LUMO) of PC₆₁BM, as well as the valence-band maximum (E_V) of perovskite and the highest occupied molecule orbital (HOMO) of PEDOT:PSS. The lower exciton binding energy will promote a favorable carrier generation and transfer channel to drift the carriers towards the PC₆₁BM and PEDOT:PSS,³⁵ and thus a better device performance.

2.5 Understanding Exciton Behavior

From the theoretical point of view, an optimal layered 2D perovskite solar cell requires a rapid photo-generated charge carrier response with nearly ballistic transportation in each layer, which requires minimized activation energy barrier of carriers determined by weakened exciton binding energy. In general, the photoluminescence spectra of layered 2D materials underly the corresponding electronic structure and excitonic states. Herein, we try to understand how the spacer cation interfere the exciton and carrier behavior by DFT calculation. Total density of states (TDOSs) demonstrates overall edge states featuring at the VBM and CBM of the host MAPbI₃ is obviously modified with the increased introduction ratio (**Figure 6a**) of long-ranged p- π polarized “rigid” amine (PEA). Projected partial density of states (PDOSs) confirms the edge states variation near the VBM and CBM can be evidently traced back to the mutual influences from PEA⁺ and BA⁺ respectively (**Figure 6b and 6c**). No extra gap states have been noticed near the Fermi level, since the HOMO and LUMO states of both PEA⁺ and BA⁺ are relatively higher than the VBM and CBM of the host. The long-ranged aromatic PEA-p- π orbitals repulsively push the excitonic states outward from the band tails resulting in narrower gaps (**Figure 6b**). Meanwhile, these Coulomb confinements induced by PEA⁺ inhibit the electronic contributions of BA⁺ towards further from the VBM and CBM of MAPbI₃ perovskite host lattice (**Figure 6c**), since those deep-HOMO and high-LUMO of BA⁺ show rather less Coulomb effects to the edge states. To verify the reliability of the model, we calculated the layered 2D perovskite bandgap (E_g) with different n values. The band gap of BA based layered 2D perovskite decreases with increasing layer number denoting a clear excitonic effect³⁶ and is in good agreement with literatures.^{12,37} (**Figure 6d**).

Consequently, the calculated E_g evolution (**Figure 6e**) of $(\text{BA,PEA})_2(\text{MA})_3\text{Pb}_4\text{I}_{13}$ increases to a peak bandgap for PEA0.125, wherein part of BA^+ is replaced by PEA^+ from the inter-layer region. Such arrangement further disturbs the local steric BA orbital alignment in the $(\text{BA,PEA})_2(\text{MA})_3\text{Pb}_4\text{I}_{13}$. While, the E_g decreases as the p- π polarized “rigid” amine cation (PEA^+) is introduced more than the ratio of 0.125, resulting from the PEA-p- π Coulomb repulsion. This is consistent with the above bandgap variation observed in the experiments (**Figure 2a**).

We now theoretically analyze the exciton binding energy variation along with the composition tuning in layered 2D materials from the view point of excitonic featured Hamiltonian³⁸:

$$E = E_g(\text{bulk}) + \frac{\pi^2 \hbar^2}{2\mu} \left(\frac{1}{R^2}\right) - 1.786 \frac{e^2}{\epsilon} \left(\frac{1}{R}\right) - 0.248 E_{RY}^* \quad (3)$$

where R is the crossover distance between the electronic and hole states estimated from the localized orbitals at the CBM and VBM. E_{RY}^* is the effective Rydberg energy, μ is the reduced mass and ϵ is the vacuum permittivity. The second term and third term represent the exciton binding energy and Coulombic interaction energy, respectively. These two terms corresponding with varying PEA^+ concentrations were calculated, as shown in **Figure 6f**. Notably, the Coulombic interaction and exciton binding energy show inverse trends. The exciton binding energy displays a decreased energetic trend initially, wherein low concentration PEA^+ introduction can spatially tune the excitonic radius and weaken the binding energy. This is in good accordance with the above temperature dependent PL experiment results. While, further increasing the PEA^+ content could result in the decreased excitonic radius and enlarged binding energy. Interestingly, although the PEA^+ energetically pins the excitonic states near the band edges and influences the E_g *via* Coulomb repulsions, the sum of the above two terms follows a similar trend with the exciton binding energy from low to medium PEA^+ concentration. Therefore, the long-ranged aromatic p- π coupling energetically tunes the exciton binding energy. However, the content of the “rigid” cation is required to optimize.

We further illustrate why the unsaturated alkylamine with long-ranged aromatic p- π coupling effect can effectively tune the corresponding excitonic radius and binding energy in $(\text{BA,PEA})_2(\text{MA})_3\text{Pb}_4\text{I}_{13}$. Accordingly, the real space orbital contour plots illustrates the hole orbitals in $(\text{BA,PEA})_2(\text{MA})_3\text{Pb}_4\text{I}_{13}$ are localized at the Pb site with fixed distance, meanwhile the localized electronic orbitals can migrate among different Pb-I sub-lattice layers (**Figure S14**). This spatial migration can be attributed to a long range (PEA-p- π)-(I-5p) coupling modulations. From this trend, PEA^+ usually induces a strong and long-range p- π orbital to flexibly tune the electronic orbital distribution, while the long chain alkylamine like BA^+ usually contributes strong dispersive hydrogen bonding to constrain the hole orbital distribution or even a tendency to confine the excitonic radius in a smaller range.

Moreover, the structural evolution of $(\text{BA,PEA})_2(\text{MA})_3\text{Pb}_4\text{I}_{13}$ as another key consideration has been summarized (**Table S4**). We have further applied an affine transformation algorithm to quantify the instantaneous influence of the PEA^+ incorporation. The initial lattice growth direction is scattered (**Figure S15a**), which can be attributed to the large mismatch of size between PEA^+ and MA^+ . The evident growth of

the longest axis has been observed due to the tight interlayer region will be greatly relaxed by the much larger PEA groups (**Figure S15b**). As more PEA entered, the growth direction becomes much concentrated, which is consistent with the mass center migration distance displays less fluctuation with higher PEA⁺ concentration (**Figure S15c**). The calculated structural evolution results support the experimental trend of relative intensity between (222) and (111) crystallographic planes in (BA,PEA)₂(MA)₃Pb₄I₁₃ perovskite that the growth direction change is more converged at high PEA⁺ ratio, as shown in **Figure 1b**. It should be mentioned that although the growth direction could be theoretically changed induced by the cations with long-range p- π coupling effect, while the formation of the orientated structure from the long chain alkylamine BA based (BA)₂(MA)₃Pb₄I₁₃ was well remained in (BA,PEA)₂(MA)₃Pb₄I₁₃ perovskite.

Thus, substituting spacer layer cation BA⁺ with a proper ratio of PEA⁺, which has long-range p- π orbital and can effectively pin the excitonic states near the band edges without changing the effective mass and introducing extra defect states, is quite efficient way to tune the exciton behaviors and photoluminescence properties.

The proposed modulation mechanism of organic spacers composed of unsaturated alkylamine cation with long-range p- π orbital coupling and long chain alkylamine cation in the layered 2D perovskite materials is shown in **Figure 6g**. BA⁺ is a long chain alkylamine cation, which suggests that BA based layered 2D perovskite can easily assemble into highly orientation structure to facilitate efficient charge transport. But PEA⁺ is a “rigid” cation with aromatic long-ranged p- π structure. The unique electronic structure of PEA can modulate exciton behaviour via tuning electronic orbital distribution. As a result, through partial introduction of PEA⁺, the exciton binding energy of modified layered 2D perovskite could be reduced, without disturbing the assembled structure. The lower exciton binding energy will promote a favorable carrier generation and transfer channel to drift the carriers towards transport layers.

3. Conclusion

In summary, for the first time, we revealed the interplay between unsaturated alkylamine with p- π coupling effect and alkylamine in layered 2D perovskite materials based on experimental characterization and DFT simulation. (BA,PEA)₂(MA)₃Pb₄I₁₃ was used as a typical example to study the corresponding crystalline phase, morphology and optoelectronic property. Combining SEM, AFM, XRD, GIWAXS, and PL results, we found that the incorporation of p- π polarized PEA cation into the 2D perovskites spacers improve carrier pathway without disturbing the orientated crystal structure. Consequently, we obtained a device with PCE of 15.46% based on (BA,PEA)₂MA₃Pb₄I₁₃ films, which is significantly improved as compared to the 11.71% based on BA₂MA₃Pb₄I₁₃. Also, the design concept of the mixed spacer cations with distinct effect is generalized to other system. It was further shown that the long chain spacer cation has superior structural flexibility to facilitate molecular self-assembly, and the unsaturated alkylamine cation with long-range p- π coupling effect further help to reduce the exciton binding energy. This work represents a rational molecule design guideline on A₁ cation in layered 2D perovskites that enables tunability on both excitonic, electronic

properties as well as the structural evolution. Continuous efforts will be focused on the investigation of the incorporation of conjugated spacer cations with electronic activity, which reduces the potential carrier barriers that improves the intrinsic optoelectronic quality of layered 2D perovskites.

4. Experimental Section

Materials Preparation: All reagents were used as received without further purification. PbI_2 (99.999%, Sigma-Aldrich), isopropanol (99.99%, Sigma-Aldrich), N,N-dimethylformamide (99.99%, Sigma-Aldrich), HI (57%, Aladdin), chlorobenzene (99.9%, Sigma-Aldrich), methanol (99.9%, Aladdin). Butyl amine and Poly (3, 4-ethylenedioxythiophene): poly (styrenesulfonate) (PEDOT:PSS), [6,6]-phenyl-C61-butyric acid methyl ester (PC_{61}BM) and bathocuproine (BCP) were purchased from Xi'an Polymer Light Technology Corp. MAI, BAI and PEAI were synthesized using the methods reported everywhere.

Device fabrication: The inverted planar heterojunction PSCs were fabricated on ITO substrates. The ITO substrates were ultrasonically cleaned with diluted detergent, deionized water, acetone, ethanol and isopropanol (IPA) in succession. The as-cleaned substrates were UV–ozone treated for 20 min. PEDOT:PSS solution was spin-coated onto the ITO substrates at 3000 rpm for 30 s, and the samples were then annealed at 120 °C for 20 min in air. The perovskite solution was comprised of BAI, PEAI, MAI and PbI_2 (2-2x : 2x : 3 : 4 molar ratio) in N,N-dimethylformamide (DMF) with concentration of 0.6 M. The perovskite precursor solution was spin-coated on the top of PEDOT:PSS modified ITO substrate at 2000 rpm for 25 s at hot atmosphere. The samples were further annealed on a hot plate at 70 °C for 20 min. Next, 30 μL of PC_{61}BM (20 mg/mL in CB) solution was then spin-coated on the top of perovskite layer at 2000 rpm for 30 s and BCP (2.5 mg/mL in methanol) was dropped onto PC_{61}BM at a rotational speed of 6000 rpm to form an electron extracting layer, and the samples were annealed on a hot plate at 70 °C for 10 min, respectively. Finally, 120 nm silver electrode was deposited via thermal evaporation under a pressure of 1×10^{-4} Pa. The active area was 0.09408 cm^2 which has been calibrated by National Institute of Metrology (NIM), China.

Characterization: The morphology were measured using a scanning electron microscope (SEM) (S4800) and atomic force microscopy (Asylum MFP-3D AFM, Asylum, USA). The XRD patterns were collected by using a PANalytical X'Pert Pro X-ray powder diffractometer with Cu $K\alpha$ radiation ($\lambda = 1.54050 \text{ \AA}$). The Grazing incidence wide angle x-ray scattering (GIWAXS) data were obtained at beamline BL14B1 of the Shanghai Synchrotron Radiation Facility (SSRF) using X-ray with a wavelength of 0.6887 \AA . Photoluminescence (PL) and temperature-dependent PL were measured by FLS980 (Edinburgh Instruments Ltd) with an excitation at 470 nm. The current density-voltage characteristics of photovoltaic devices were obtained using a Keithley 2400 source-measure unit. The photocurrent was measured under AM1.5G illumination at 100 mW/cm^2 under a Newport Thermal Oriel 91192 1000 W solar simulator at room temperature in air. The J–V results were obtained with slow scan rate of 40 mV s^{-1} with 0.02 V step and 0.5 s delay time. External quantum efficiencies were measured by an Enli Technology (Taiwan) EQE measurement system.

Calculation Setup: We used the CASTEP package to perform DFT calculations³⁹. For the functional, we choose the Perdew-Burke-Ernzerhof based generalized gradient approximation (GGA)⁴⁰⁻⁴² to describe the electronic exchange-correlation interaction. The Broyden-Fletcher-Goldfarb-Shannon (BFGS) algorithm has been chosen to minimize the residue of the Hellmann-Feynman forces until converges to meet limitation of 0.001 eV/Å of the geometry optimization. The convergence tolerances of the total energy and the inter-ionic displacement have been constrained within 5×10^{-5} eV per atom and 0.005 Å per atom, respectively. The original $(\text{BA}_{1-x}\text{PEA}_x)_2(\text{MA})_2\text{Pb}_4\text{I}_{13}$ model has been built based on the XRD experimental data⁴³, in which the BA molecule will be gradually replaced by PEA molecule from $x=0.1$ to $x=1$ concentration. To accelerate the computation speed and optimize the computational cost for the large cell modelling, ultrasoft pseudopotential scheme has been chosen⁴⁴. We choose different orbital projectors for different atoms to represent their valence states, which we treated (1s), (2s, 2p), (2s, 2p), (5s, 5p), (5d,6s,6p) as the valence states for H, C, N, I and Pb, respectively. Hence, with this setting, the planewave cut-off energy for the basis set establishment can be minimized to around 380 eV. The Monkhost-Pack reciprocal space integration was performed by separation parameter of 0.07 \AA^{-1} to balance between accuracy and computation time consumption, which was also self-consistently suggested by total energy minimization⁴⁵. Based on the special k -points sampling settings, the total energy is converged within the maximum expected self-consistent cycles.

For the mass center location of distorted structure, the affine transformation matrix method has been applied. Assuming the shape of the cell is initially a cube and given the parameters of the cell size and angle, we can extrapolate where any given atom would be positioned within a Euclidean space using affine transformations. The affine transformation takes any set of coordinates and transposes them to a new position within the coordinate space, using a process of rotation, transposition and scaling. Practically this is achieved using matrix multiplication with a homogeneous coordinate matrix and a transformation matrix. Importantly, because we can preserve the origin for each set of coordinates for any given parameter set, we can readily calculate how the cell shapes differ given their parameters.

Supporting Information

Supporting Information is available from the Wiley Online Library or from the author.

Acknowledgements

This work is supported by National Natural Science Foundation of China (51722201) (51672008) (91733301), National Key Research and Development Program of China Grant No. 2017YFA0206701, Natural Science Foundation of Beijing, China (Grant No. 4182026), Young Talent Thousand Program. The authors would like to thank Dr. Haipeng Xie for UPS measurement.

Received: ((will be filled in by the editorial staff))

Revised: ((will be filled in by the editorial staff))

Published online: ((will be filled in by the editorial staff))

References

1. Yusoff, A. R. b. M.; Nazeeruddin, M. K., *Adv. Energy Mater.* **2018**, *8*, 1702073.
2. National renewable energy laboratory, Best research-cell efficiency chart, <https://www.nrel.gov/pv/assets/images/efficiency-chart.png>
3. Chen, Q.; De Marco, N.; Yang, Y.; Song, T.-B.; Chen, C.-C.; Zhao, H.; Hong, Z.; Zhou, H.; Yang, Y., *Nano Today* **2015**, *10*, 355.
4. Green, M. A.; Ho-Baillie, A., *ACS Energy Lett.* **2017**, *2*, 822.
5. Sum, T. C.; Mathews, N., *Energy Environ. Sci.* **2014**, *7*, 2518.
6. Chen, J.; Cai, X.; Yang, D.; Song, D.; Wang, J.; Jiang, J.; Ma, A.; Lv, S.; Hu, M. Z.; Ni, C., *J. Power Sources* **2017**, 355, 98.
7. Li, F.; Liu, M., *J. Mater. Chem. A* **2017**, *5*, 15447.
8. Leijtens, T.; Eperon, G. E.; Noel, N. K.; Habisreutinger, S. N.; Petrozza, A.; Snaith, H. J., *Adv. Energy Mater.* **2015**, *5*, 1500963.
9. Kim, H. S.; Seo, J. Y.; Park, N. G., *ChemSusChem* **2016**, *9*, 2528.
10. Asghar, M.; Zhang, J.; Wang, H.; Lund, P., *Renew. Sust. Energ. Rev.* **2017**, *77*, 131.
11. Smith, I. C.; Hoke, E. T.; Solis-Ibarra, D.; McGehee, M. D.; Karunadasa, H. I., *Angew. Chem. Int. Edit.* **2014**, *53*, 11232.
12. Cao, D. H.; Stoumpos, C. C.; Farha, O. K.; Hupp, J. T.; Kanatzidis, M. G., *J. Am. Chem. Soc.* **2015**, *137*, 7843-50.
13. Tsai, H.; Nie, W.; Blancon, J. C.; Stoumpos, C. C.; Asadpour, R.; Harutyunyan, B.; Neukirch, A. J.; Verduzco, R.; Crochet, J. J.; Tretiak, S.; Pedesseau, L.; Even, J.; Alam, M. A.; Gupta, G.; Lou, J.; Ajayan, P. M.; Bedzyk, M. J.; Kanatzidis, M. G.; Mohite, A. D., *Nature* **2016**, *536*, 312.
14. Zhang, X.; Wu, G.; Yang, S.; Fu, W.; Zhang, Z.; Chen, C.; Liu, W.; Yan, J.; Yang, W.; Chen, H., *Small* **2017**, *13*, 1700611.
15. Fu, W.; Wang, J.; Zuo, L.; Gao, K.; Liu, F.; Ginger, D. S.; Jen, A. K. Y., *ACS Energy Lett.* **2018**, *3*, 2086.
16. Hong, X.; Ishihara, T.; Nurmikko, A. V., *Phys. Rev. B* **1992**, *45*, 6961.
17. Tsai, H.; Asadpour, R.; Blancon, J. C.; Stoumpos, C. C.; Even, J.; Ajayan, P. M.; Kanatzidis, M. G.; Alam, M. A.; Mohite, A. D.; Nie, W., *Nat. Commun.* **2018**, *9*, 2130.
18. Zhang, X.; Ren, X.; Liu, B.; Munir, R.; Zhu, X.; Yang, D.; Li, J.; Liu, Y.; Smilgies, D.-M.; Li, R.; Yang, Z.; Niu, T.; Wang, X.; Amassian, A.; Zhao, K.; Liu, S., *Energy Environ. Sci.* **2017**, *10*, 2095.
19. Zhou, N.; Shen, Y.; Li, L.; Tan, S.; Liu, N.; Zheng, G.; Chen, Q.; Zhou, H., *J. Am. Chem. Soc.* **2018**, *140*, 459.
20. Long, M.; Zhang, T.; Chen, D.; Qin, M.; Chen, Z.; Gong, L.; Lu, X.; Xie, F.; Xie, W.; Chen, J.; Xu, J., *ACS Energy Lett.* **2019**, *4*, 1025.
21. Lian, X.; Chen, J.; Qin, M.; Zhang, Y.; Tian, S.; Lu, X.; Wu, G.; Chen, H. *Angew. Chem. Int. Ed.* **2019**, DOI: 10.1002/ange.201902959.
20. Liao, Y.; Liu, H.; Zhou, W.; Yang, D.; Shang, Y.; Shi, Z.; Li, B.; Jiang, X.; Zhang, L.; Quan, L. N.; Quintero-Bermudez, R.; Sutherland, B. R.; Mi, Q.; Sargent, E. H.; Ning, Z., *J. Am. Chem. Soc.* **2017**, *139*,

6693.

21. Liu, J.; Leng, J.; Wu, K.; Zhang, J.; Jin, S., *J. Am. Chem. Soc.* **2017**, *139*, 1432.
22. Ross, R. T., *J. Chem. Phys.* **1967**, *46*, 4590.
23. Braly, I. L.; Hillhouse, H. W., *J. Phys. Chem. C* **2016**, *120*, 893.
24. Zhou, N.; Shen, Y.; Zhang, Y.; Xu, Z.; Zheng, G.; Li, L.; Chen, Q.; Zhou, H., *Small* **2017**, *13*, 1700484.
25. Xiao, X.; Dai, J.; Fang, Y.; Zhao, J.; Zheng, X.; Tang, S.; Rudd, P. N.; Zeng, X. C.; Huang, J., *ACS Energy Lett.* **2018**, *3*, 684.
26. Chong, W. K.; Thirumal, K.; Giovanni, D.; Goh, T. W.; Liu, X.; Mathews, N.; Mhaisalkar, S.; Sum, T. C., *Phys. Chem. Chem. Phys.* **2016**, *18*, 14701.
27. Kitazawa, N.; Aono, M.; Watanabe, Y., *Mater. Chem. Phys.* **2012**, *134*, 875.
28. Gauthron, K.; Lauret, J.; Doyennette, L.; Lanty, G.; Al Choueiry, A.; Zhang, S.; Brehier, A.; Largeau, L.; Mauguin, O.; Bloch, J., *Opt. Express* **2010**, *18*, 5912.
29. Gan, L.; Li, J.; Fang, Z.; He, H.; Ye, Z., *J. Phys. Chem. Lett.* **2017**, *8*, 5177.
30. Zhang, W.; Saliba, M.; Stranks, S. D.; Sun, Y.; Shi, X.; Wiesner, U.; Snaith, H. J., *Nano Lett.* **2013**, *13*, 4505.
31. Qin, L.; Lv, L.; Li, C.; Zhu, L.; Cui, Q.; Hu, Y.; Lou, Z.; Teng, F.; Hou, Y., *RSC Adv.* **2017**, *7*, 15911.
32. Kong, W.; Ye, Z.; Qi, Z.; Zhang, B.; Wang, M.; Rahimi-Iman, A.; Wu, H., *Phys. Chem. Chem. Phys.* **2015**, *17*, 16405.
33. Poglitsch, A.; Weber, D., *J. Chem. Phys.* **1987**, *87*, 6373.
34. Wu, K.; Bera, A.; Ma, C.; Du, Y.; Yang, Y.; Li, L.; Wu, T., *Chem. Chem. Phys.* **2014**, *16*, 22476.
35. Sun, S.; Salim, T.; Mathews, N.; Duchamp, M.; Boothroyd, C.; Xing, G.; Sum, T. C.; Lam, Y. M., *Energy Environ. Sci.* **2014**, *7*, 399.
36. Mao, L.; Ke, W.; Pedesseau, L.; Wu, Y.; Katan, C.; Even, J.; Wasielewski, M. R.; Stoumpos, C. C.; Kanatzidis, M. G., *J. Am. Chem. Soc.* **2018**, *140*, 3775.
37. Stoumpos, C. C.; Cao, D. H.; Clark, D. J.; Young, J.; Rondinelli, J. M.; Jang, J. I.; Hupp, J. T.; Kanatzidis, M. G., *Chem. Mater.* **2016**, *28*, 2852.
38. Haug, H. & Koch, S. W. *Quantum Theory of the Optical and Electronic Properties of Semiconductors*. 5 edn, **2009**.
39. Clark, S. J.; Segall, M. D.; Pickard, C. J.; Hasnip, P. J.; Probert, M. I.; Refson, K.; Payne, M. C., *Z. Krist.-Cryst. Mater.* **2005**, *220*, 567.
40. Perdew, J. P.; Burke, K.; Ernzerhof, M., *Phys. Rev. Lett.* **1996**, *77*, 3865.
41. Perdew, J. P.; Wang, Y., *Phys. Rev. B* **1992**, *45*, 13244.
43. Stoumpos, C. C.; Cao, D. H.; Clark, D. J.; Young, J.; Rondinelli, J. M.; Jang, J. I.; Hupp, J. T.; Kanatzidis, M. G., *Chem. Mater.* **2016**, *28*, 2852.
44. Vanderbilt, D., *Phys. Rev. B* **1990**, *41*, 7892.
45. Probert, M.; Payne, M., *Phys. Rev. B* **2003**, *67*, 075204.

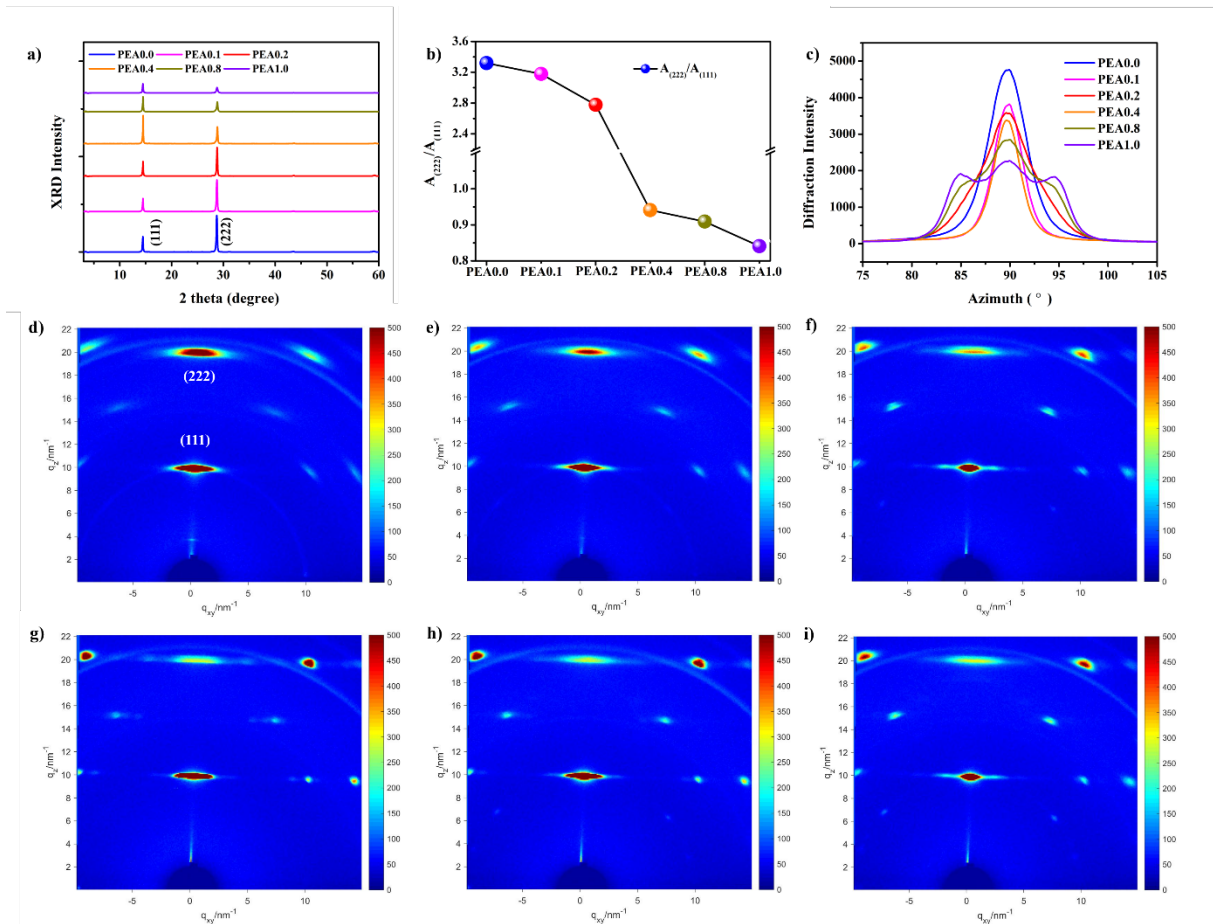


Figure 1. (a) XRD patterns of the $(\text{BA},\text{PEA})_2(\text{MA})_3\text{Pb}_4\text{I}_{13}$ films, respectively; (b) Integral diffraction peak area of (222)/(111) as a function of PEA ratio; (c) Integrated intensity plots azimuthally along the ring at $q_{xy} \sim -0.25 \text{ \AA}^{-1}$ to 0.25 \AA^{-1} ; (d)-(i) GIWAXS patterns of the perovskite films of $(\text{BA}_{1-x}\text{PEA}_x)_2(\text{MA})_3\text{Pb}_4\text{I}_{13}$ ($x=0, 0.1, 0.2, 0.4, 0.8$ and 1.0) films, respectively.

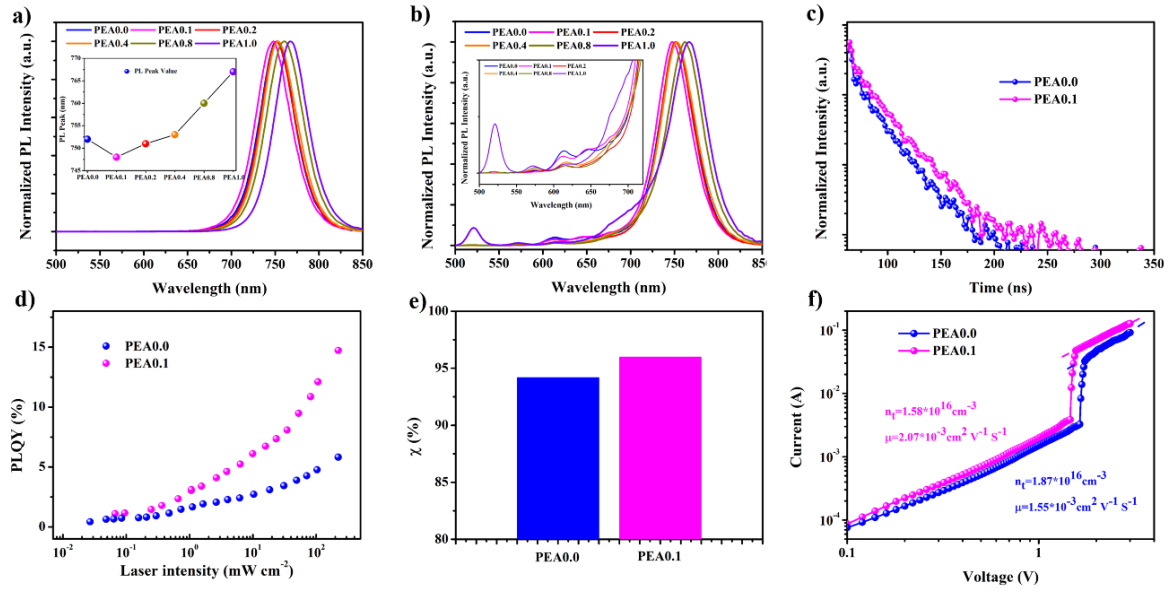


Figure 2. (a) The steady-state PL spectra of the (BA,PEA)₂(MA)₃Pb₄I₁₃ series layered 2D perovskite films from front side; (b) from back (glass substrate) side; (c) TRPL spectra for ITO/ PEA0.0 and PEA0.1 perovskite films; (d) PLQY measurements of PEA0.0 and PEA0.1 based film at various laser intensity; (e) Material quality parameter (χ) denoting optoelectronic quality (calculated from PLQY and bandgap); (f) Dark current–voltage measurements of the electron-only devices for the PEA0.0 and PEA0.1 perovskite.

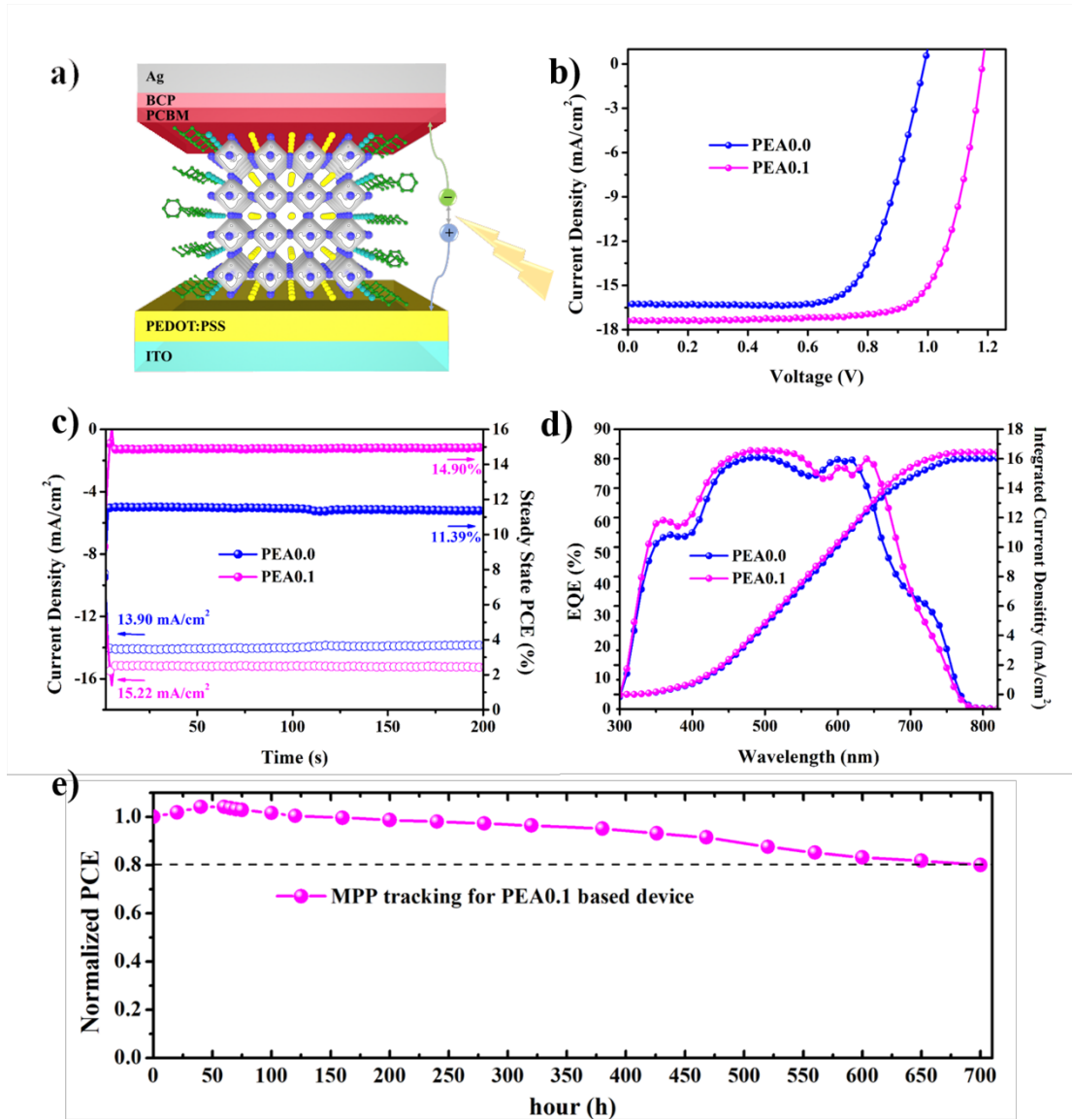


Figure 3. (a) Device structure of the layered 2D perovskite solar cell; (b) The best J-V curve; (c) The steady-state PCE; (d) EQE spectra of PEA0.0 and PEA0.1 based perovskite solar cell; (e) Stability test at maximum power point (MPP) under continuous light illumination for the un-encapsulated PEA0.1 based device stored in N₂ environment.

Table 1. Summary of the device performance of PEA0.0 and PEA0.1 based solar cells.

Device	V _{oc} (V)	J _{sc} (mA/cm ²)	PCE (%)	FF (%)
BA ₂ MA ₃ Pb ₄ I ₁₃	0.988	16.11	11.71	73.56
(BA _{0.9} PEA _{0.1}) ₂ MA ₃ Pb ₄ I ₁₃	1.182	17.12	15.46	76.40

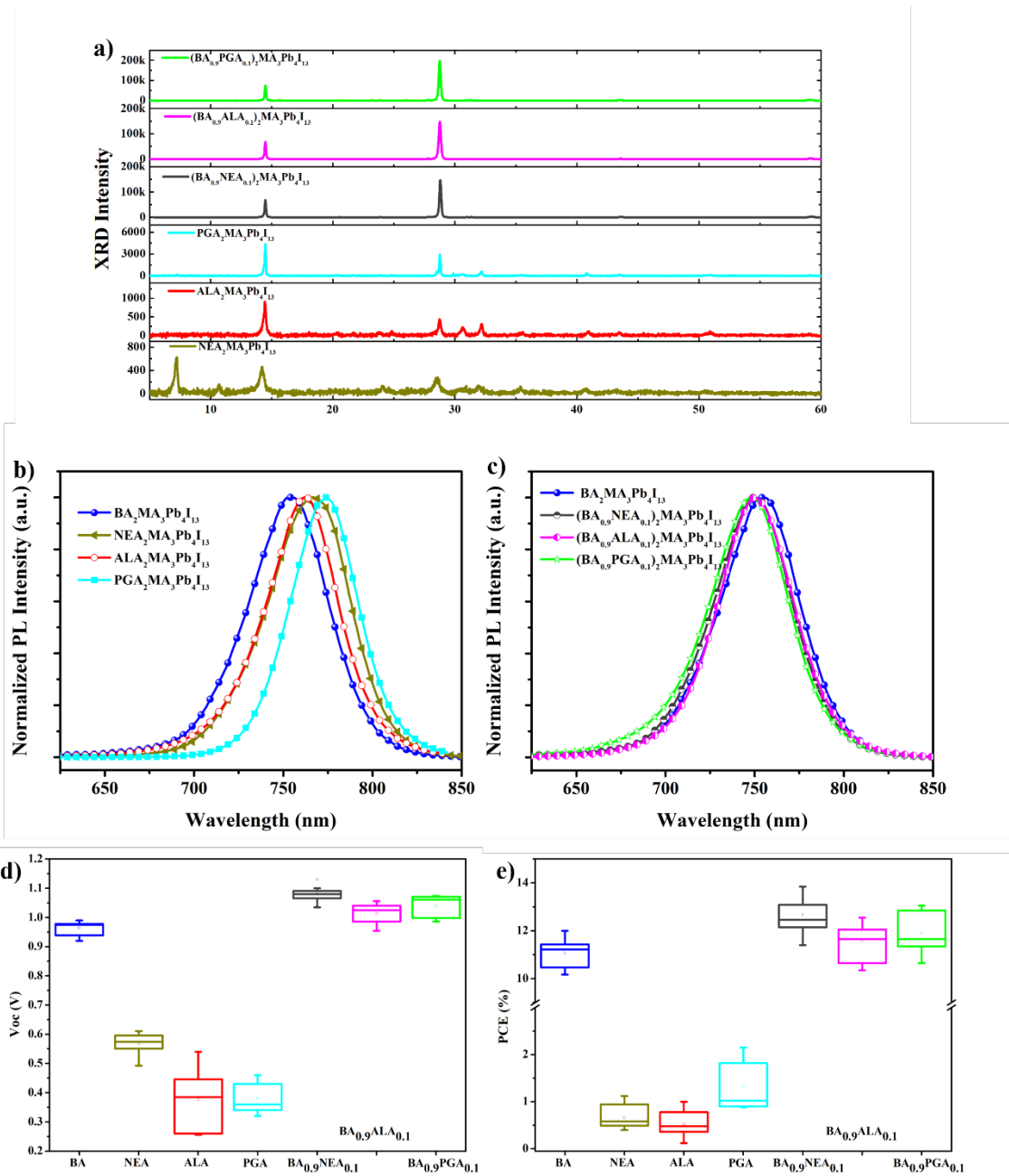


Figure 4. The characterization of NEA, ALA, PGA, $\text{BA}_{0.9}\text{NEA}_{0.1}$, $\text{BA}_{0.9}\text{ALA}_{0.1}$, $\text{BA}_{0.9}\text{PGA}_{0.1}$. (a) XRD patterns; (b) and (c) The steady-state PL spectra; (c) V_{oc} and (d) PCE statistic distribution.

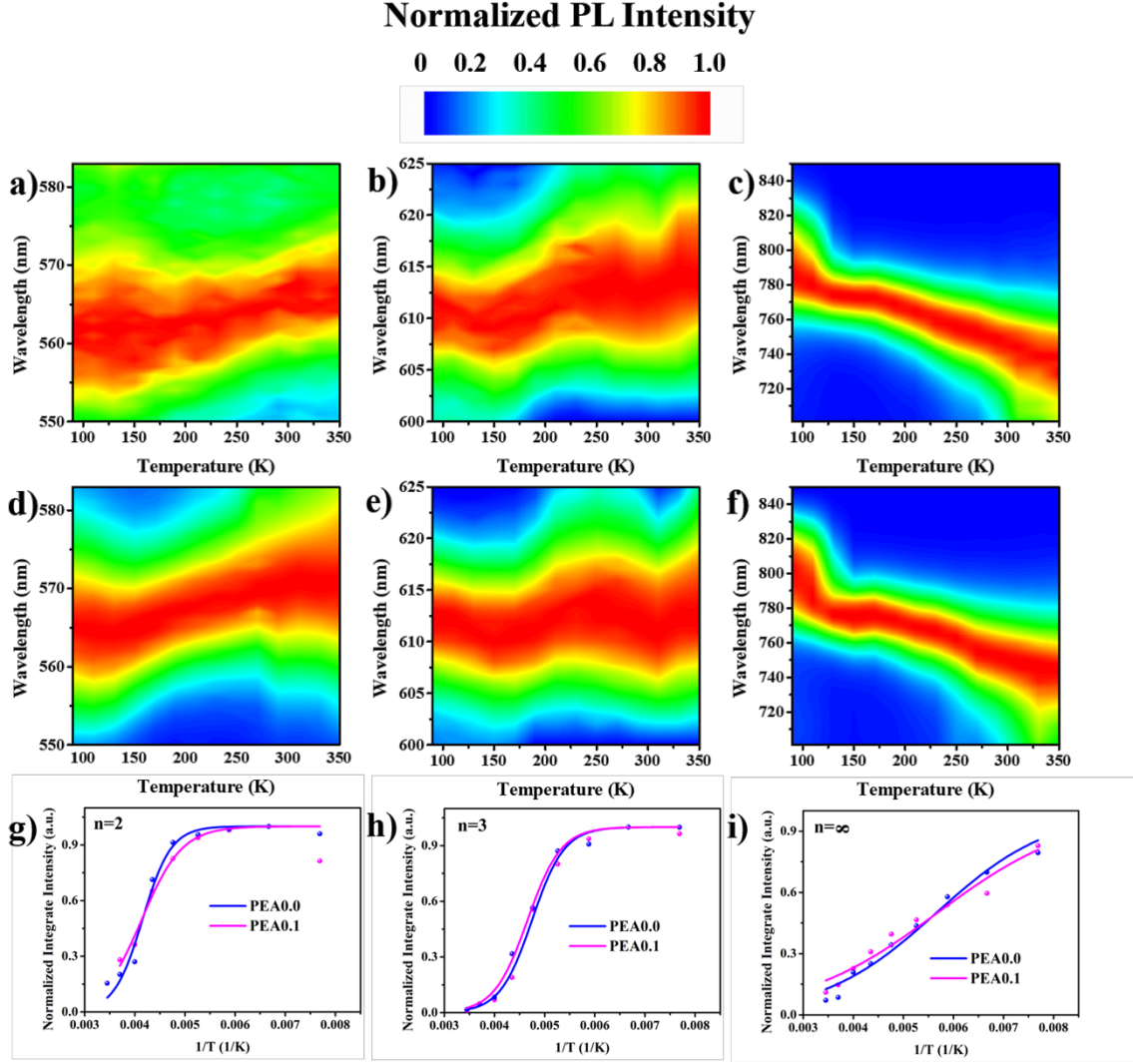


Figure 5. (a) and (d) Temperature-dependent PL mapping of n=2 phase for PEA0.0 and PEA0.1, respectively; (b) and (e) n=3 phase; (c) and (f) n=∞ phase; (g)-(i) Temperature dependent data of integrated intensity of n=2, n=3, and n=∞ phase, respectively.

Table 2. The summarized exciton binding energy of different n values fitted by Equation (1) according to Figure 5g-i.

Exciton Binding Energy	PEA0.0 (meV)	PEA0.1 (meV)
n=2	303.2	256.5
n=3	269.8	243.5
n=∞	75.3	61.7

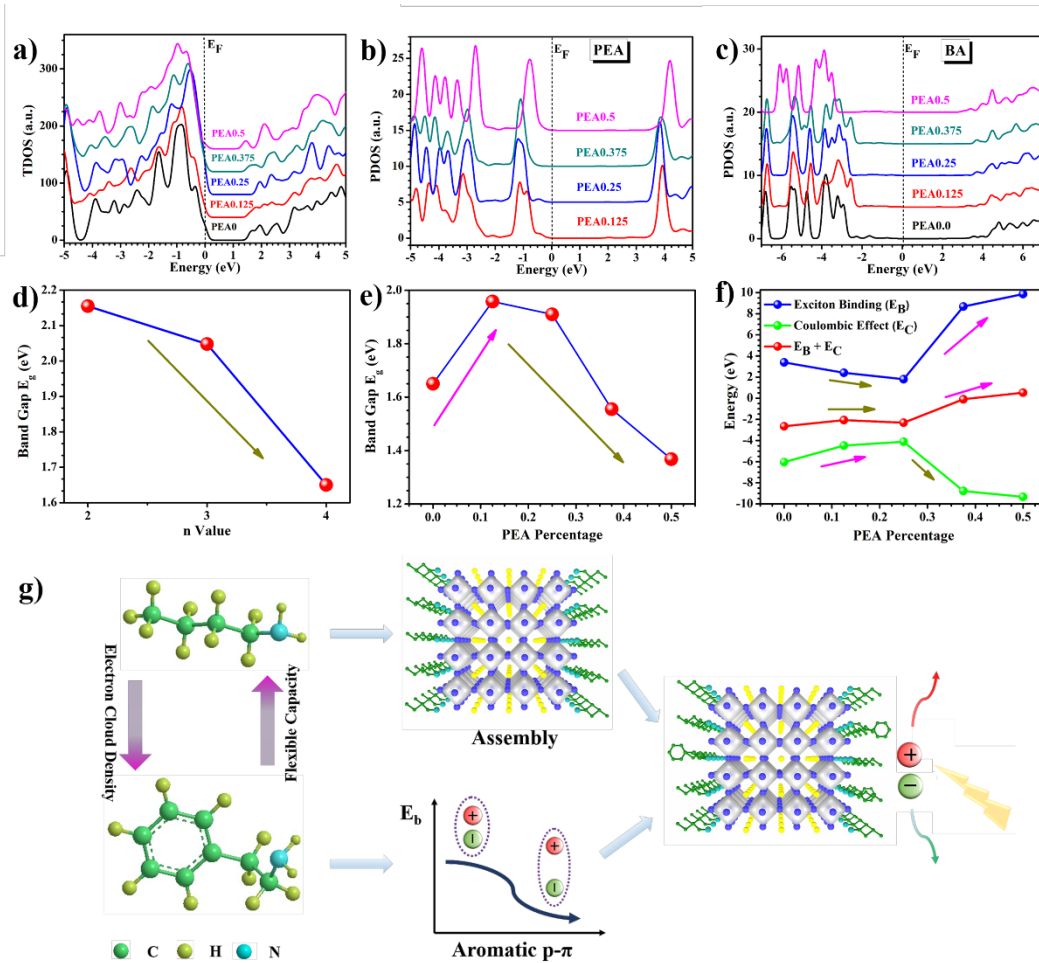


Figure 6. (a) Total density of states (TDOSs) for the overall layered perovskite with related to the PEA percentage; (b) Projected partial density of states (PDOSs) for the electronic contributions of different percentage of PEA⁺ within the inter-layer region of perovskite; (c) PDOSs for the electronic contributions of BA⁺ with related to different percentage of PEA⁺ within the inter-layer region of perovskite; (d) The band gap variation with the layer number n ; (e) The band gap variation with PEA percentage; (f) The variation of exciton binding energy and Coulombic interaction energy with PEA⁺ percentage; (g) Schematic illustration of mechanism via PEA⁺ introduction into BA based layered perovskite.